Available online at www.sciencedirect.com

International Journal of Heat and Fluid Flow 25 (2004) 729–740

International Journal of HEAT AND FLUID FLOW

www.elsevier.com/locate/ijhff

Heat transfer in a laminar separation bubble affected by oscillating external flow

J.G. Wissink [a,*], V. Michelassi [b], W. Rodi [a]

[a] *Institute for Hydromechanics, University of Karlsruhe, Kaiserstrasse 12, Karlsruhe 76128, Germany*
[b] *GE Nuovo Pignone, Via Felice Matteucci 2, 50127 Florence, Italy*

Received 9 January 2004; accepted 21 April 2004
Available online 28 July 2004

Abstract

A three-dimensional Direct Numerical Simulation (DNS) of passive heat transfer in a Laminar Separation Bubble (LSB) over a flat plate affected by oscillating external flow is presented. The oscillation imposes a periodicity which is employed for phase-averaging. The flat plate is kept at a uniform, low temperature. The local Nusselt number, *Nu*, is determined as a function of phase. In the dead-air region of the bubble *Nu* is found to be relatively small, while it peaks in the recirculation region where hot outer fluid gets entrained and is transported towards the flat plate. Each period a new separation bubble is formed, that merges with the old separation bubble. The reverse flow inside the separation bubble reaches values of up to 60% of the local free-stream velocity, which is sufficient to make the separation bubble absolutely unstable such that self-sustained turbulence can exist. For the phase-averaged flow, neither the turbulent viscosity hypothesis nor the temperature gradient-diffusion hypothesis is found to hold.

1. Introduction

A strong enough adverse pressure gradient will cause a laminar boundary layer over a solid surface to separate resulting in a Laminar Separation Bubble (LSB). The separated boundary layer is very unstable and will usually undergo rapid transition to turbulence. An oscillating external flow alternately enhances and reduces the adverse pressure gradient such that the location of separation and the location of transition move back and forth. Previously, DNS of LSB-flow with constant free-stream has been performed by Alam and Sandham (2000), Maucher et al. (1997, 1999), Spalart and Strelets (2000) and Wissink and Rodi (2002). The geometry employed in Wissink and Rodi (2002) is identical to the one employed in the present simulation and was chosen in accordance with experiments performed by Metin Talan of Prof. Hourmouziadis' group (Lou and Hourmouziadis, 2000) at the Technical University of Berlin. Without explicitly adding disturbances, Spalart and Strelets (2000) and Wissink and Rodi (2002) observed transition via a 2D Kelvin–Helmholtz (KH) instability of the shear layer, most likely triggered by numerical roundoff error. The KH-instability manifested itself by the quasi-periodic shedding of spanwise rolls of fluctuating flow.

In an earlier simulation of a LSB with oscillating oncoming flow without heat transfer (Wissink and Rodi, 2003a,b) (Simulation A in Table 1) the amplitude and period of the oscillating oncoming flow were approximately twice as large as the amplitude and period employed in the present simulation (Simulation B in Table 1). In Simulation A, each period a new separation bubble was obtained that moved downstream some time after the outer flow started to accelerate. Considerable time was found to be needed between the onset of inflow-deceleration and the actual shedding of the first roll of recirculating, turbulent flow. From this, we may conclude that the period, $P = 0.61L/U_0$, employed in this simulation, though significantly longer than the mean period $P_{\mathrm{KH}} = 0.0714L/U_0$ associated with the KH instability observed by Wissink and Rodi (2002), is still too short for the typical quasi periodic vortex shedding to establish itself. The periodic motion was found to cause a pattern of turbulent patches separated by "becalmed" flow. A similar pattern was observed along

---

[*] Corresponding author. Tel.: +49-721-608-3536; fax: +49-721-661-686.
E-mail address: wissink@ifh.uni-karlsruhe.de (J.G. Wissink).

0142-727X/$ - see front matter © 2004 Elsevier Inc. All rights reserved.
doi:10.1016/j.ijheatfluidflow.2004.04.005

Table 1
Overview of the simulations performed

Simulation	Grid	Size span	Amplitude	Period	Inflow temperature
A	966×226×128	0.12L	0.20	$0.61L/U_0$	–
B	966×226×128	0.12L	0.10	$0.30L/U_0$	$1.38T_0$
B.1	1286×310×128	0.08L	0.10	$0.30L/U_0$	$1.38T_0$

the suction side of turbine blades, where the impingement of periodic oncoming wakes induces small, localised areas of turbulent flow (see also Wissink (2003) and the references therein). When the oncoming flow is hotter than the flat plate, the entrainment of outer fluid into the separation bubble and the turbulence generated at a later stage both greatly enhance passive heat transfer towards the flat plate. These effects also play a role in a real turbine, where it is vital that the heat transfer from the hot outer flow towards the blade is not excessively large. DNS data can be of great help to understand the physical mechanisms involved and to improve models for passive heat transfer. Hence, a DNS of passive heat transfer in a LSB-flow affected by oscillating external flow is carried out as part of the German Research Foundation (DFG) project "Periodic Unsteady Flow in Turbomachinery" (see Simulation B in Table 1). Along with the passive heat transfer, we also aim to study the effects of a change in the amplitude and period of the inflow on the dynamics of the LSB flow downstream. Therefore, in Simulation B it was decided to reduce the period and amplitude compared to the ones employed in Simulation A. The reduction in period also allowed us to perform phase-averaging over significantly more phases than in Simulation A, without increasing the computational costs.

The present paper reports on a simulation of the idealised situation of separated flow over a flat plate, which is kept at a constant temperature, in the presence of hot, oscillating oncoming flow. Passive heat transfer effects will be discussed and a comparison with the earlier simulation without passive heat transfer, reported in Wissink and Rodi (2003a,b), will be presented.

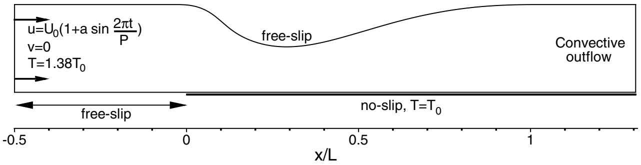

Fig. 1. Geometry of the flow problem.

1.1. Computational details

In the present DNS with passive heat transfer, as in the experiments (Lou and Hourmouziadis, 2000), the adverse pressure gradient was induced by the special shape of the upper wall (see Fig. 1). To limit the number of grid-points, free-slip boundary conditions for the velocity combined with an adiabatic boundary condition for the temperature were applied along this boundary. Along the flat plate, no-slip boundary conditions for the velocity field and a constant temperature $T = T_0$ were prescribed. Along the lower boundary, upstream of the flat plate an adiabatic boundary condition for the temperature was combined with a free-slip boundary condition for the velocity. Wiggles that originate from the stagnation point at $x/L = 0$ were explicitly removed; At the lower free-slip boundary, every time-step the velocities were filtered in the streamwise direction, using $\hat{\mathbf{u}} = \frac{1}{2}(\mathbf{u}(x,0,z) + \mathbf{u}(x-\Delta x,0,z))$, where Δx is the local size of the mesh in the x-direction. At the outlet, a convective boundary condition was applied, while at the inlet a fixed temperature $T = 1.38T_0$, which is typical for turbomachinery flow with cooling, combined with an oscillating flow

$$(u,v,w) = U_0\left(1 + a\sin\frac{2\pi t}{P}, 0, 0\right),$$

were prescribed. Here U_0 is the mean inlet velocity, $P = 0.30$ is the period and $a = 0.10$ is the amplitude of the oscillating flow. As a dimensionless measure of the local heat transfer to the plate, h, the Nusselt number is introduced:

$$Nu = \frac{hL}{k} = \frac{-T_0}{T_0 - 1.38T_0}\frac{\partial(T/T_0)}{\partial(y/L)}\bigg|_{\text{wall}} \approx 2.63\frac{\partial(T/T_0)}{\partial(y/L)}\bigg|_{\text{wall}},$$

where T_0 and L are defined above and k is the thermal conductivity of air. The Reynolds number of the flow problem, based on U_0 and L (see Fig. 1) is $Re = 60000$. The computational mesh and Reynolds number are in fact identical to the ones employed earlier in Simulation A (Wissink and Rodi, 2003a,b) (see Table 1). As already noted above, in this earlier simulation, both the amplitude and the period of the oncoming flow were approximately twice as large as the ones employed in Simulation B which is presented here. In Wissink and Rodi (2003a,b) (WR) it was shown that the 966×226×128 point mesh employed in Simulation A is sufficient to obtain a good qualitative description of the LSB flow and a good quantitative representation of important phase-averaged quantities like the location of separation, the size of the separation bubble, the maximum reverse flow etc. Since the smaller amplitude and period employed in Simulation B leads to a LSB flow that is somewhat less demanding on the computational grid, it was decided to adopt the finest mesh used in WR for Simulation B too. A third simulation (B.1) on a $1286\times310\times128$ mesh is performed to further study the quality of the results obtained with Simulation B.

The computations were performed using a second order accurate finite volume discretisation of the three-dimensional incompressible Navier–Stokes equations combined with a convection-diffusion equation for the temperature in which the Prandtl number of air, $Pr = 0.71$, is employed. Time-integration was performed using a three-stage Runge–Kutta method using 6400 equal time-steps per period P. For a more detailed description of the numerical method employed see Breuer and Rodi (1996). The simulations were run on the IBM SP-SMP at the Computing Centre of the University of Karlsruhe using 60 processors in Simulations A and B and 128 processors in Simulation B.1. In Simulations B and B.1, phase-averaged statistics are gathered during 20 periods. Each period is divided into 256 equal phases, $\phi = 0, \ldots, \frac{255}{256}$. During phase-averaging, statistics are also averaged in the homogeneous, spanwise direction. Before commencing the phase-averaging, the flow is allowed to develop for 10 periods. In Table 1 an overview is presented of the simulations that are compared. To identify time, ϕ is used for phase-averaged quantities and t/T is used for instantaneous quantities.

2. Results

To assess the quality of Simulation B, in Fig. 2 the time-averaged shape factor H and the time-averaged skin-friction coefficient C_f have been plotted for Simulations B and B.1. The graphs of H are found to be in good agreement. In both simulation the maximum, $H_{\max}$, is reached at $x/L = 0.518$, which indicates that the time-averaged separation bubble is located at the same position in both simulations. The maximum H reached in Simulation B.1 is $H_{\max} = 10.3$ compared to $H_{\max} = 10.8$ in Simulation B. This difference is very likely a consequence of the reduced grid size in the spanwise direction as employed in Simulation B.1, which is better able to resolve spanwise modes that eventually destroy the initially two-dimensional re-circulation region.

Note that the reduced spanwise size in Simulation B.1 is still sufficient to accommodate several of the large spanwise structures visible in Fig. 6, it is therefore not very likely that it adversely affects the presence of large spanwise modes. For $x/L < 0.75$, a very good agreement is obtained between Simulations B and B.1 for the time-averaged skin-friction coefficient C_f. For instance, the size and location of the two regions with negative C_f-values, corresponding to reverse flow regions, are identical. This implies that the location, size and structure of the time-averaged LSB is grid-independent. For $x/L > 0.75$, the agreement between Simulations B and B.1 becomes slightly worse for both H as well as C_f. Though the difference in resolution between Simulations B and B.1, respectively, will account for some of the differences observed for $x/L > 0.75$, the main problem is thought to be the limited amount of 20 periods of phase-averaging that has been performed. To obtain well-converged turbulence statistics in this wake-like flow region, with a large re-circulating roll of turbulent flow passing through it every period, one would need considerably more phase-averaging periods than what was considered reasonable from a computational costs point of view. In Fig. 3 space-time contours of the phase-averaged friction velocity are plotted to identify the phase-dependent evolution of the area of flow separation. The figure shows that in both Simulations A and B each period a new separation bubble is generated as the old one is convected downstream. Compared to Simulation A, in Simulation B, owing to the reduced amplitude and period, the separation bubble that first appears at $\phi \approx 0.25$ only exhibits moderate expansion in the upstream and downstream direction. While in Simulation A the separation bubble reaches its most upstream location $x/L \approx 0.33$ at $\phi \approx 0.68$, in Simulation B the most upstream location, $x/L \approx 0.35$, is reached at $\phi \approx 0.62$. For $\phi > 0.9$, both simulations show the existence of two regions upstream of $x/L = 0.6$, labelled I and II, respectively, where the flow separates. In both Simulations, Region I corresponds to the roll of turbulent

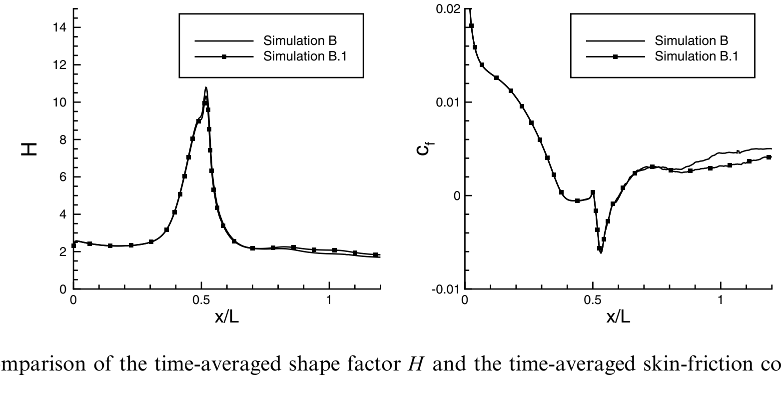

Fig. 2. Comparison of the time-averaged shape factor H and the time-averaged skin-friction coefficient C_f.

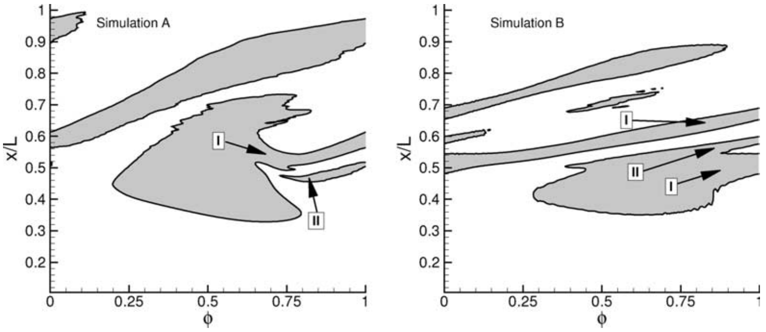

Fig. 3. Space-time plots of the area of separation. The grey area is identified with negative phase-averaged friction velocity.

flow that is shed just before the entire separation bubble starts to move downstream (see snapshots at $t/P = 8.5$ in Figs. 5 and 6), while Region II corresponds to the recirculation region of the remainder of the separation bubble (see also Fig. 7). Observe that while in Simulation A the remainder of the old separation bubble (Region II) stays clear from the newly generated separation bubble, in Simulation B the two merge, giving the false impression that Region II is generated inside the new separation bubble. Despite the difference in oscillation amplitude and period, in both simulations the roll of turbulent recirculating flow induces flow separation for a considerable time after its original creation. By monitoring the location of Region I in Simulations A and B, respectively, the downstream movement of the separation bubble can be easily tracked. The temporal merging of the remainder of the old recirculation zone and the newly formed recirculation zone in Simulation B allows for a considerable amount of fluctuations to become entrained in the new bubble, thereby eventually fostering the turbulence generated in Region I. The separation in the area around $(\phi, x/L) \approx (0.5, 0.7)$, observed in Simulation B, is a recirculation "revival" of Region II induced by the maximum in the adverse streamwise inflow-pressure gradient reached at $\phi = 0.5$.

The maximum phase-averaged reverse flow, u_{rev}, as a percentage of the maximum phase-averaged outer flow at the same streamwise location, has been plotted in Fig. 4 (left) as a function of phase, together with the actual streamwise location where this maximum is reached. The figure clearly illustrates a major difference between simulations A and B; While the u_{rev} graph reaches a peak of $u_{\text{rev}} \approx 130\%$ at $\phi \approx 0.74$ in Simulation A, in Simulation B the peak of $u_{\text{rev}} \approx 60\%$ is located at $\phi \approx 0.20$. The difference in size of the two peaks is most likely a consequence of the difference in amplitude of the corresponding inflow signal, while the phase-shift observed is very likely caused by the difference in period of the inflow signals.

The time interval between the onset of inflow deceleration at $\phi = 0.25$ and the reverse flow reaching its peak is found to be approximately the same ($\Delta t \approx 0.30$ time-units) in both simulations. The slow decay in u_{rev}, observed in Simulation B for $0.25 < \phi < 0.75$ is most likely a consequence of the inflow-deceleration in this interval, a process that favours separation and hence the increase of reverse flow and is responsible for the fact that the maximum reverse flow never falls beneath $u_{\text{rev}} = 20\%$, which, according to Alam and Sandham (2000), implies that the corresponding LSB flow remains absolutely unstable and hence self-sustained turbulence can exist. Similarly, the rapid decline in the peak for $\phi > 0.75$ in Simulation A is very likely caused by inflow acceleration promoting the decline of reverse flow.

In Fig. 4 (right), the Nusselt number, *Nu*, is plotted at four different phases, $\phi = 0, 0.25, 0.50, 0.75$. Except for the region around $x/L \approx 0.43$, where the flow tends to separate, the relatively high values of *Nu* reflect the fact

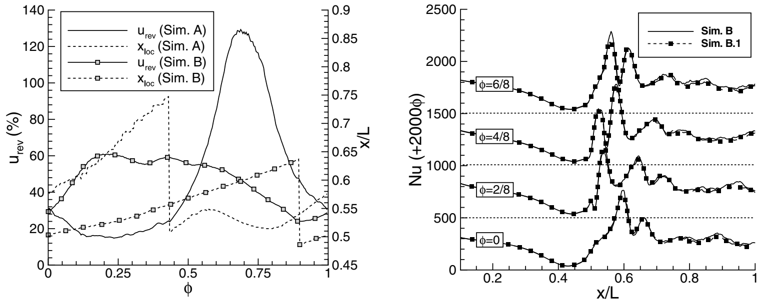

Fig. 4. Left: maximum reverse flow together with its location for Simulations A and B. Right: (Simulations B and B.1) Nusselt number at four phases $\phi = 0, 0.25, 0.50, 0.75$.

that convection is dominant as often observed in turbomachinery flows. The thickening of the laminar boundary layer from the leading edge to $x/L \approx 0.35$, is reflected in a gradual decrease of *Nu*. The local maxima observed at all four phases correspond to recirculation regions where hot outer fluid is entrained and subsequently convected towards the flat plate (see also Fig. 3 (right)). Turbulent fluctuations present downstream of $x/L \approx 0.55$ promote the exchange of heat between the outer fluid and the flat plate and inhibit the Nusselt number to drop below $Nu \approx 240$ (see also Fig. 5). The phase-averaged Nusselt numbers obtained in Simulation B and Simulation B.1 are generally found to be in good agreement. Only at $\phi = 0$ and $\phi = 6/8$, the maximum *Nu* in Simulation B.1 is slightly smaller than its counterpart in Simulation B. As the slightly reduced maximum shape-factor in Simulation B.1 (see Fig. 2), this is likely to be a consequence of the increased resolution of spanwise modes in Simulation B.1 promoting the breakdown of the initially predominantly 2D re-circulation region. This faster breakdown of the re-circulation will lead to a slightly smaller flux of hot outer fluid towards the flat plate thereby decreasing *Nu*. The four pairs of snapshots plotted in Fig. 5, provide an impression of the evolution of the magnitude of the vorticity, $\|\omega\|$, and the normalised temperature, T/T_0,

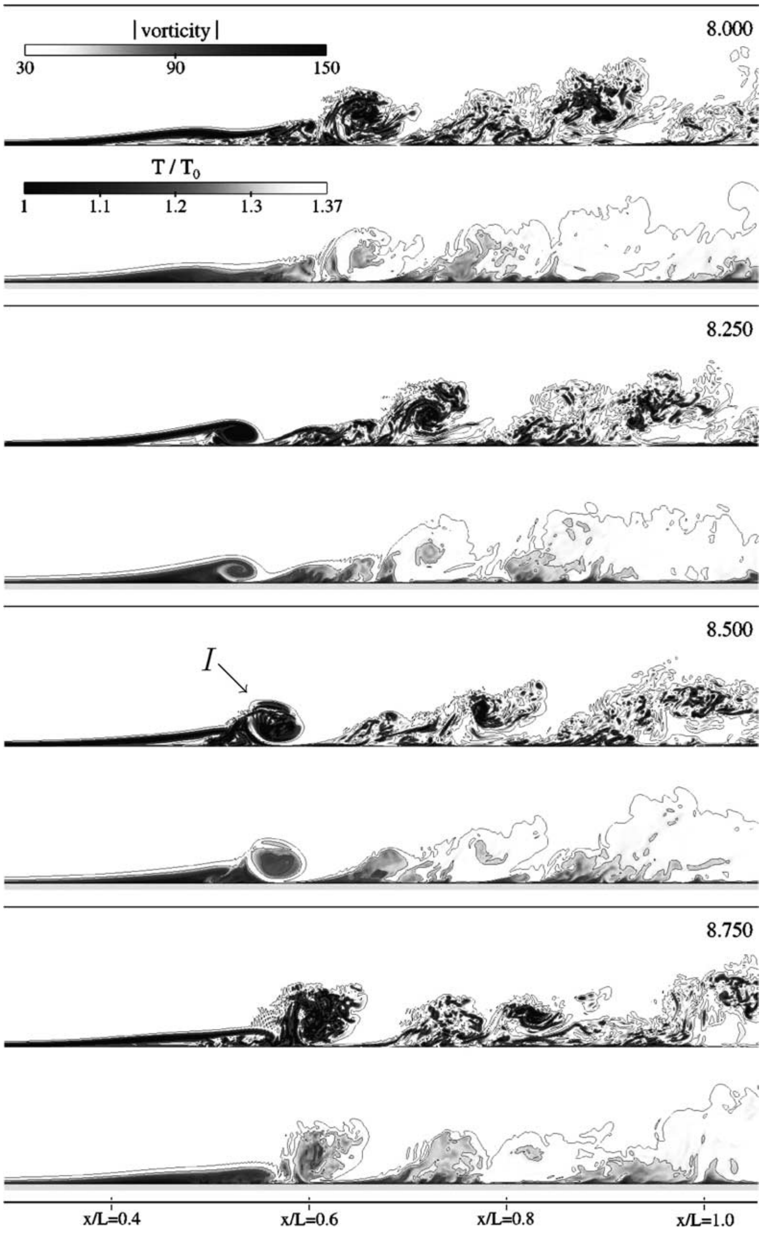

Fig. 5. Simulation B: snapshots at $t/P = 8.00$, 8.25, 8.50, 8.75 showing contours of the magnitude of the instantaneous vorticity $\|\omega\|$ and the temperature T/T_0 at mid-span.

during one phase. At first sight, the pictures show quite a good correlation between the two quantities, especially in the laminar region. Even though vorticity is not a passive scalar, this is to be expected since both quantities are introduced into the main flow by diffusion at the boundary and are subsequently convected by the near-wall flow field. At the latest stage when the vorticity field becomes three-dimensional, the interaction between the flow-field and the vorticity field due to vortex-stretching is found to diminish the correlation. For instance, in the regions where the flow is turbulent, local concentrations of vorticity can be found that are not matched by local concentrations of temperature. The latter is illustrated by comparing the vorticity-field and the temperature field in Fig. 5 for $x/L > 0.7$.

The boundary layer dynamics are illustrated by the four snapshots of the instantaneous spanwise vorticity shown in Fig. 6. The snapshots cover one typical period, P, of inflow oscillation. Between $t/P = 8.00$ and 8.25, the separated boundary layer rolls up, and is subsequently shed at $t/P \approx 8.50$. The shed roll of turbulent flow, corresponding to Region I in Fig. 3 (right), is clearly visible in the snapshot taken at $t/P = 8.75$. An impression of its subsequent downstream movement can be obtained in the snapshots at $t/P = 8.00$ and 8.25, which in fact display the spanwise roll of turbulent flow that is shed in the previous cycle of inflow oscillation. Region II, displayed in Fig. 3 (right), corresponds to the small spanwise roll of turbulent flow labelled ‘‘II’’, immediately upstream of $x/L = 0.60$, in the snapshot at $t/P = 8.00$. Observe that, as in Simulation A (WR), the snapshots indicate the presence of turbulent patches separated by regions of ‘‘becalmed’’ flow. The figure illustrates that most fluctuations are generated inside the recirculation zones. As a consequence, the distribution of heat inside the recirculation zones tends to become uniform very quickly as also witnessed in Fig. 5 at $t/P = 8.50$ and $x/L \approx 0.57$.

In Fig. 7 contours of the phase-averaged fluctuating kinetic energy are shown at four phases, corresponding to the snapshots plotted in Figs. 5, 6. The area corresponding to the large roll of turbulent flow that is shed every period is marked ‘‘I’’, while the remainder of the recirculation region of the old separation bubble, that was found to merge with the newly formed bubble is marked ‘‘II’’ (see also Fig. 3). Significant production of fluctuating kinetic energy commences inside the region of recirculating flow, somewhat prior to $\phi = 0.25$,

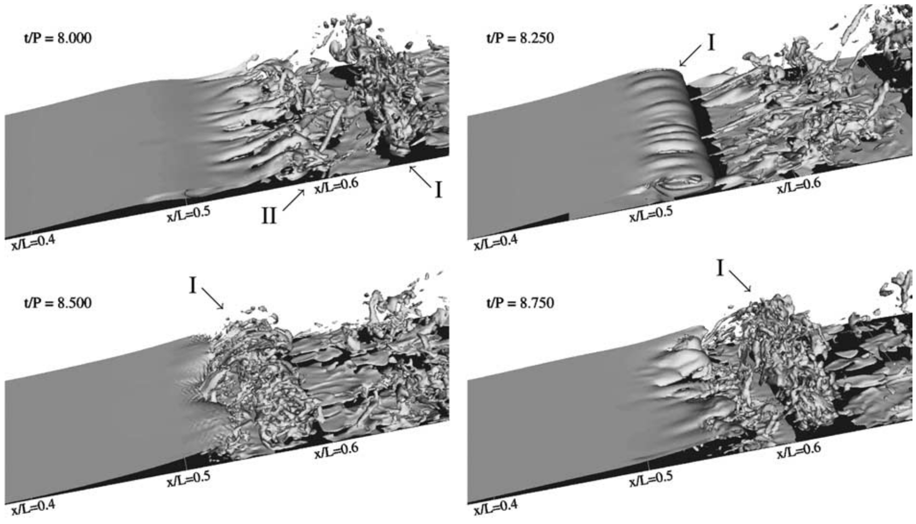

Fig. 6. Simulation B: snapshots at $t/P = 8.00$, 8.25, 8.50, 8.75 of iso-surfaces of the spanwise vorticity $\omega_z = -150U_0/L$.

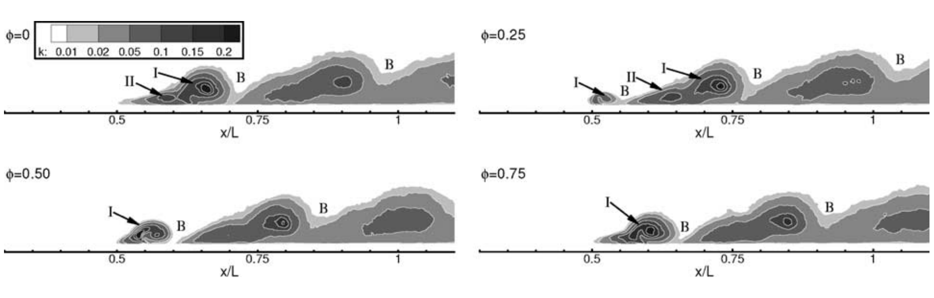

Fig. 7. Simulation B: phase-averaged fluctuating kinetic energy at four phases.

which, according to Fig. 3, is close to the phase where u_{rev} reaches its maximum. At $\phi = 0.25$, the recirculating flow is still attached to the separated boundary layer (see Fig. 6), though the flow separation pattern in Fig. 3 suggests that the roll is already shed. From this we may conclude that it is dangerous to draw conclusions about the topology of the separated shear layer solely based on local information along the flat plate boundary. Note that Fig. 7 also shows that at $\phi = 0$ turbulence is not only generated in Region I but also in Region II. The areas marked "B" correspond to regions of becalmed flow as already observed in Fig. 6. The location of the becalmed regions do not necessarily correspond to minima of Nu. Instead, convection of hot outer fluid towards the flat plate inside such a becalmed region may result in a significant increase in Nu, e.g. at $\phi = 0$, the peak near $x/L = 0.7$ in Fig. 4 (right) corresponds to the most upstream region of becalmed flow in Fig. 6.

The frequency distribution of the v-velocity component at various locations inside the time-averaged shear layer is shown in Fig. 8 for Simulation A (left) and Simulation B.1 (right). The period of the oscillating inflow induces a basis frequency of $f_b \approx 1.64$ for Simulation A and $f_b \approx 3.33$ for Simulation B.1, respectively. The peaks in the frequency distributions correspond to the respective basis frequencies of the simulations and their higher harmonics. At the point located farthest downstream, P_4, the graphs show that in both simulations the most unstable Kelvin–Helmholz mode has a frequency of $f \approx 6.7$ and that the instability is triggered by a higher harmonic of the oscillating inflow's frequency.

The turbulent Prandtl number, σ_{T}, is defined as the ratio $\nu_{\mathrm{T}}/\Gamma_{\mathrm{T}}$ of the turbulent viscosity and the turbulent heat diffusivity. According to the gradient-diffusion hypothesis, the turbulent transport of T is down the mean scalar gradient, that is: a positive value Γ_{T} exists such that

$$\overline{\mathbf{u}'T'} = -\Gamma_{\mathrm{T}}\nabla\overline{T} \tag{1}$$

holds, where $\mathbf{u} = (u, v, w)^t = (u_1, u_2, u_3)^t$, $\overline{\mathbf{u}'T'}$ corresponds to the covariance of $\mathbf{u}$ and T and $\overline{T}$ corresponds to the phase-averaged value of T. To check whether the two vectors $\overline{\mathbf{u}'T'}$ and $\nabla\overline{T}$ are really aligned,

$$\varepsilon = \frac{\|\overline{\mathbf{u}'T'} + |\Gamma_{\mathrm{T}}|\nabla\overline{T}\|}{\|\overline{\mathbf{u}'T'}\|}$$

is calculated, where

$$\Gamma_{\mathrm{T}} = -\frac{\overline{\mathbf{u}'T'} \cdot \nabla\overline{T}}{\nabla\overline{T} \cdot \nabla\overline{T}} \tag{2}$$

and the 2-norm $\|\cdot\|$ of the vector u_i is defined by $\|u_i\| = \sqrt{u_i u_i}$. The two vectors are perfectly aligned and have opposite direction when $\varepsilon = 0$, they are orthogonal when $\varepsilon = 1$ and they are aligned and of the same direction when $\varepsilon = 2$. In other words, we have down-gradient diffusion when $\varepsilon < 1$ and countergradient diffusion for $\varepsilon > 1$. The latter case would require a negative eddy diffusivity Γ_{T} so that the concept breaks down.

As illustrated in Fig. 9, for the phase-averaged flow at $\phi = 0$ only in small (black) regions the gradient diffusion hypothesis (1) holds. On the other hand, regions of countergradient diffusion — labelled "C" — are found where approximately $\overline{\mathbf{u}'T'} = a\nabla\overline{T}$ holds for some postive a. The "distribution" of ε changes from one phase to another, though the imperfect alignment and the existence of regions with countergradient diffusion, such as illustrated at $\phi = 0$, is typical for all phases. The lack of smoothness in the contours plotted in Fig. 9 is most

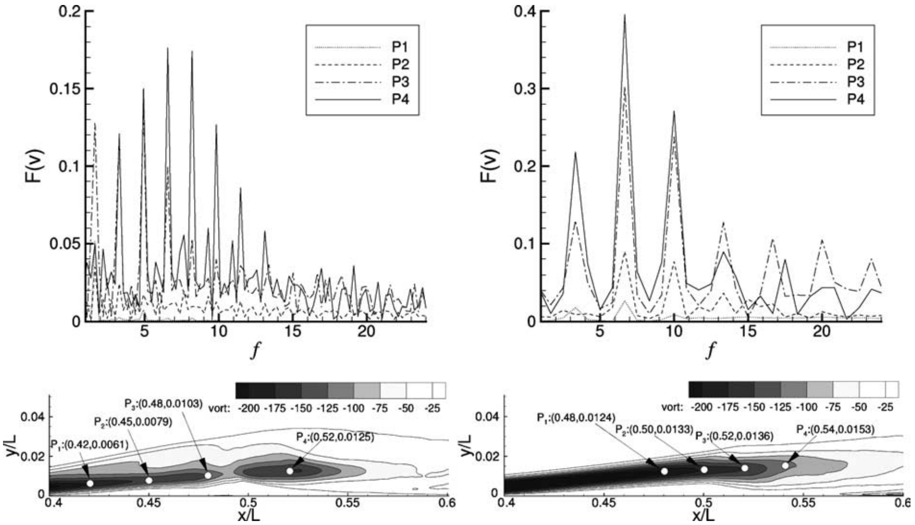

Fig. 8. Frequency spectrum of v at points P_1, P_2, P_3 and P_4 located in the time-averaged shear layer. The frequency f has been made dimensionless using the mean inflow velocity U_0 and L (see also Figure 1). The location of P_1, P_2, P_3 and P_4 is identified in the lower graphs showing contours of the mean spanwise vorticity. Left: Simulation A, Right: Simulation B.1.

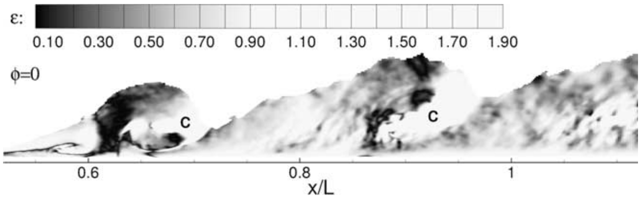

Fig. 9. Simulation B: Alignment of $\overline{\mathbf{u}'T'}$ and $\nabla\overline{T}$ ranging from a perfect alignment with opposite sense of direction for $\varepsilon = 0$ via orhogonality for $\varepsilon = 1$, to a perfect alignment with the same sense of direction for $\varepsilon = 2$ (regions labelled "C"). Value blanking is used where the spanwise fluctuation, $\overline{w'w'}$, is less than 0.005.

likely due to the limited number of 20 periods during which phase-averaging is performed. While in definition (2) a projection of $\mathbf{u}'T'$ on $\nabla\overline{T}$ is used to determine Γ_T, alternatively Γ_T can be defined as

$$\Gamma_T^1 = \frac{\|\overline{\mathbf{u}'T'}\|}{\|\nabla\overline{T}\|}, \tag{3}$$

where $\|\cdot\|$ is the 2-norm, also used in the definition of ε above. When $\mathbf{u}'T'$ and $\nabla\overline{T}$ are perfectly aligned and have opposite sense of direction, definitions (2) and (3) will give the same value for Γ_T, otherwise differences are likely to occur.

Note that the goal of the value blanking for $\overline{w'w'} < 0.005$, as employed in Figs. 9–13, is to identify and show only those regions in which the flow is (mildly) turbulent. In the remainder of the computational domain fluctuations are negligible and the gradient diffusion hypothesis (1) as well as the turbulent-viscosity hypothesis (4) are void.

The turbulent-viscosity hypothesis states that the deviatoric Reynolds' stress is proportional to the mean rate of strain, that is

$$-\overline{u_i'u_j'} + \frac{2}{3}k\delta_{ij} = 2\nu_T S_{ij} = \nu_T\left(\frac{\partial\overline{u}_i}{\partial x_j} + \frac{\partial\overline{u}_j}{\partial x_i}\right). \tag{4}$$

The scalar turbulent viscosity ν_T assumed in this expression can be conveniently calculated using

$$\nu_T = \frac{\|\frac{2}{3}k\delta_{ij} - \overline{u_i'u_j'}\|}{\|2S_{ij}\|}, \tag{5}$$

where the 2-norm $\|\cdot\|$ of the matrix a_{ij} is defined by $\|a_{ij}\| = \sqrt{a_{ij}a_{ij}}$. Note that since the spanwise direction is homogeneous, $\overline{u_1'u_3'} = \overline{u_2'u_3'} = S_{13} = S_{23} = S_{33} = 0$ holds. Because of that, these stresses together with $-\overline{u_3'u_3'} + \frac{2}{3}k$, which according to (4) is proportional to S_{33}, are discarded.

To describe turbulent boundary layer flows with Reynolds Averaged Navier Stokes (RANS) models of

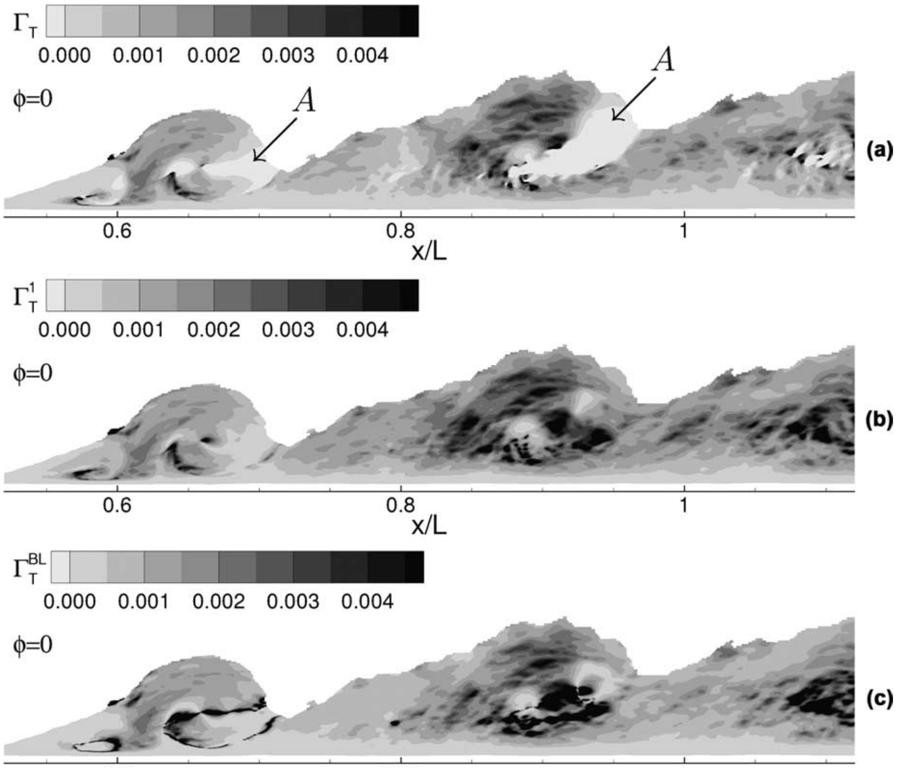

Fig. 10. Simulation B: comparison of Γ_T (a), Γ_T^1 (b) and Γ_T^{BL} (c) for the phase-averaged flow at $\phi = 0$, value blanking is used where the spanwise fluctuation, $\overline{w'w'}$, is less than 0.005.

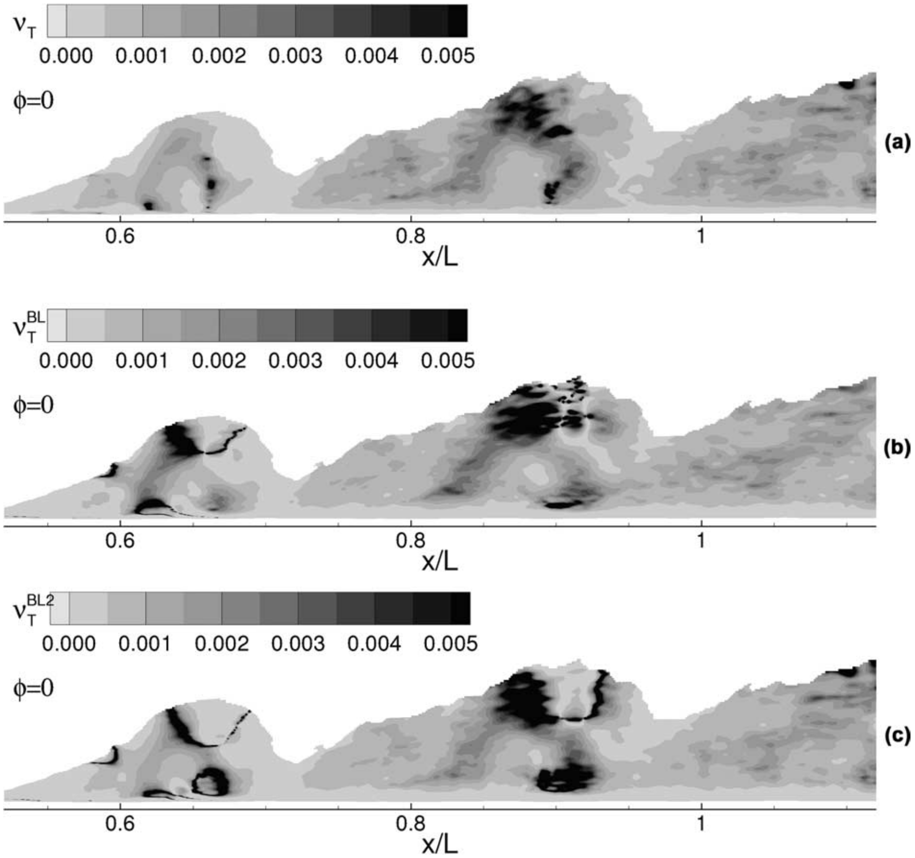

Fig. 11. Simulation B: comparison of ν_T (a), ν_T^{BL} (b) and ν_T^{BL2} (c) for the phase-averaged flow at $\phi = 0$, value blanking is used where the spanwise fluctuation, $\overline{w'w'}$, is less than 0.005.

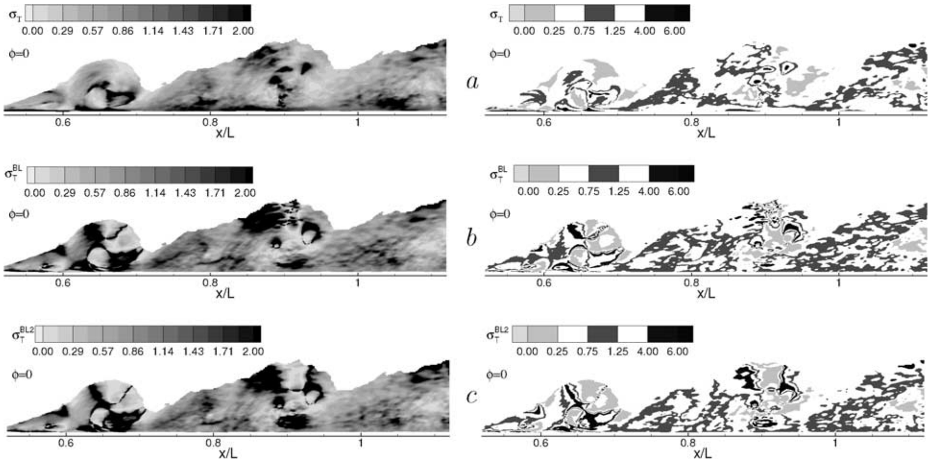

Fig. 12. Simulation B: comparison of σ_T (a), σ_T^{BL} (b) and σ_T^{BL2} (c) for the phase-averaged flow at $\phi = 0$, value blanking is used where the spanwise fluctuations, $\overline{w'w'}$, are less than 0.005.The left plots are reiterated on the right to highlight three contours, $\sigma_T < 0.25$, $0.75 < \sigma_T < 1.25$ and $\sigma_T > 4$, separated by white regions.

the eddy-viscosity type, the turbulent heat diffusivity is defined by

$$\Gamma_T^{BL} = -\frac{\overline{v'T'}}{\frac{\partial \overline{T}}{\partial y}}, \qquad (6)$$

while the turbulent viscosity is defined by

$$\nu_T^{BL} = -\frac{\overline{u'v'}}{\frac{\partial \overline{u}}{\partial y}}. \qquad (7)$$

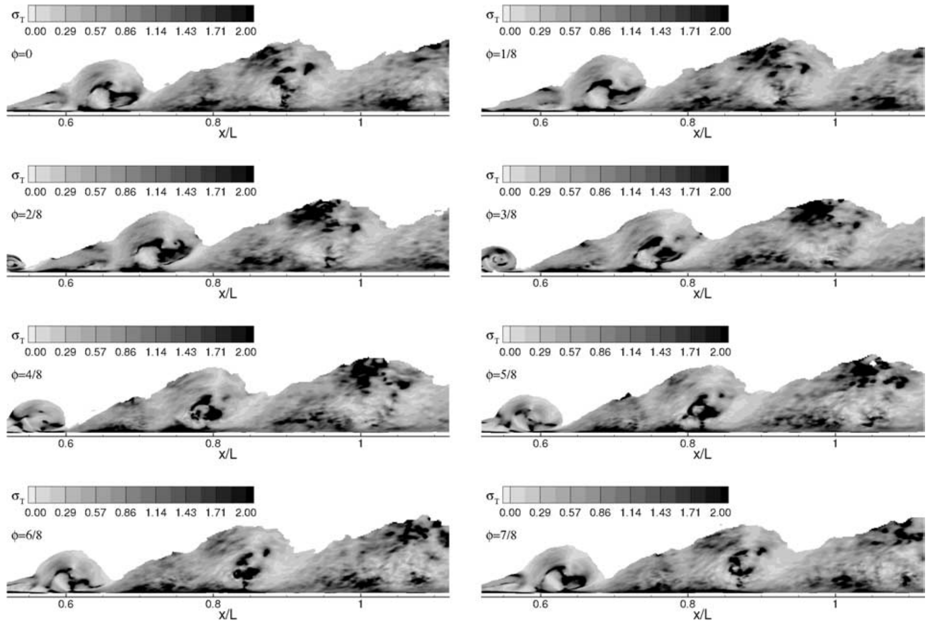

Fig. 13. Simulation B: contours of the phase-averaged turbulent Prandtl number at eight phases, $\phi = 0, 1/8, 2/8, \ldots, 7/8$, value blanking is used where the spanwise fluctuation $\overline{w'w'}$, is less than 0.005.

$\Gamma_{\rm T}$, defined in (2), $\Gamma_{\rm T}^{1}$, defined in (3) and $\Gamma_{\rm T}^{\rm BL}$, defined in (6) are compared in Fig. 10. Since in Fig. 9 it was already illustrated that (1) generally does not hold, it is to be expected that differences can be observed when comparing the contour plots of $\Gamma_{\rm T}$ on the one side to $\Gamma_{\rm T}^{1}$ and $\Gamma_{\rm T}^{\rm BL}$ on the other side. Most notable are differences occurring in regions near $x/L \approx 0.7$ and $x/L \approx 0.95$, identified by arrows labelled "A", where high values of $\Gamma_{\rm T}^{1}$ and $\Gamma_{\rm T}^{\rm BL}$ are reached compared to relatively small values of $\Gamma_{\rm T}$, which are due to the existence of countergradient diffusion in these regions (see also Fig. 9). In general, Fig. 10(b) and (c) show fair agreement. However, small regions do exist where $\Gamma_{\rm T}^{1}$ reaches high values compared to $\Gamma_{\rm T}^{\rm BL}$, indicating that $-\frac{\overline{u'T'}}{\frac{\partial \overline{T}}{\partial x}}$ is more important than $-\frac{\overline{v'T'}}{\frac{\partial \overline{T}}{\partial y}}$, and conversely other regions exist where $\Gamma_{\rm T}^{\rm BL}$ reaches high values compared to $\Gamma_{\rm T}^{1}$ $\left(-\frac{\overline{v'T'}}{\frac{\partial \overline{T}}{\partial y}} \text{ is more important than } -\frac{\overline{u'T'}}{\frac{\partial \overline{T}}{\partial x}}\right)$.

In Fig. 11, the turbulent viscosities $\nu_{\rm T}$, defined in (5), $\nu_{\rm T}^{\rm BL}$, defined in (7) and $\nu_{\rm T}^{\rm BL2}$ defined by

$$\nu_{\rm T}^{\rm BL2} = -\frac{\overline{u'v'}}{\frac{\partial \overline{u}}{\partial y} + \frac{\partial \overline{v}}{\partial x}},$$

are compared. The differences observed between $\nu_{\rm T}^{\rm BL}$ and $\nu_{\rm T}^{\rm BL2}$ illustrate that $\frac{\partial \overline{v}}{\partial x}$ is not always negligible with respect to $\frac{\partial \overline{u}}{\partial y}$. The fact that the two contour plots of $\nu_{\rm T}$ and $\nu_{\rm T}^{\rm BL2}$, respectively, are not identical, indicates that the turbulent viscosity hypothesis does not hold everywhere in the turbulent region. For instance, in Fig. 11(c) dark regions near $x/L = 0.9$ with high values of turbulent viscosity are clearly visible, while in Fig. 11(a) these regions are virtually absent, indicating that in these regions one or both of the diagonal terms S_{11} and S_{22} of the mean rate of strain tensor are more important than the off-diagonal term S_{12}.

The differences observed between the various contour plots shown in Figs. 10 and 11, are also reflected in the contour plots of the turbulent Prandtl number shown in Fig. 12. Here, the turbulent Prandtl number $\sigma_{\rm T}$ (a) obtained with (3) and (5) is compared to the turbulent Prandtl number $\sigma_{\rm T}^{\rm BL}$ (b) obtained with (6) and (7) and with $\sigma_{\rm T}^{\rm BL2}$ (c) obtained with (6) and $\nu_{\rm T}^{\rm BL2}$. To be better able to judge the range of values assumed by the turbulent Prandtl number, the plots in the left part of the figure are again displayed at the right hand side, this time showing only three contours separated by white regions. The light grey contours correspond to $\sigma_{\rm T} < 0.25$, the medium grey contours represent $0.75 < \sigma_{\rm T} < 1.25$ and the dark grey contours correspond to values $\sigma_{\rm T} > 4.0$, respectively. Usually, a turbulent Prandtl number of $\sigma_{\rm T} = 0.9$ is used in RANS simulations of boundary layer flows. This value is valid for the inner layer of a thermal boundary layer. For the outer layer of a wall flow or a free shear layer values of $\sigma_{\rm T} = 0.5$ can be reached (Cebeci and Bradshaw, 1984). All plots indicate that only in a relatively small part of the turbulent region $\sigma_{\rm T}$ assumes values near 0.9. In most of the turbulent region $\sigma_{\rm T}$ is smaller than 0.9. However, the average of $\sigma_{\rm T}$ over the entire area where $\overline{w'w'} > 0.005$ results in values of $0.87 \leqslant \overline{\sigma_{\rm T}} \leqslant 0.93$ for the phase-averaged mean Prandtl number $\overline{\sigma_{\rm T}}$. A subsequent averaging of $\overline{\sigma_{\rm T}}$ over all phases gives a mean value of $\langle \sigma_{\rm T} \rangle = 0.90$, indicating that the approximation used in RANS simulations of boundary layers is also valid for the present flow problem. In general, a large variation in σ_T is observed, reflected in an overall variance of about 3.95. Hence, it is unlikely that assuming that σ_T is constant everywhere would result in correct predictions by a RANS simulation. In the light-grey regions mentioned above, where $\sigma_T < 0.25$, the temperature diffusivity Γ_T is significantly larger than the turbulent viscosity. This is for instance observed inside the rolled-up shear layer in the region adjacent to the flat plate near $x/L = 0.65$ where Γ_T assumes values typical for the surrounding area, while the turbulent viscosity is at least a factor four smaller (see also Figs. 10 and 11). The darker areas, where $\sigma_T > 4$, are rather small. Comparing the plots in Fig. 12 to one another, shows a slight increase in dark areas in the plots displayed in (b) and (c) compared to the ones shown in (a).

For the sake of completeness, in Fig. 13 the phase-averaged turbulent Prandtl number at eight different phases is displayed. Since it was shown above that neither the turbulent viscosity hypothesis nor the temperature gradient-diffusion hypothesis generally holds, it was decided to use as much available information as possible for the calculation of σ_T. That is: σ_T is calculated using (3) and (5). As illustrated in Fig. 13, during neither of the eight phases σ_T assumes a value near 0.9 in the entire turbulent region. What is interesting to note, though, is that peaks of σ_T, corresponding to dark regions, are clearly convected downstream with the main flow structures. As the regions are convected downstream, they slowly disintegrate owing to diffusion. High values of σ_T are reached in those areas where ν_T is notably larger than Γ_T. This could for instance indicate that a temperature-wise well-mixed region exhibits a large production of turbulence, for instance due to the presence of small regions of high shear, entrained in the re-circulation zone of the separation bubble. It is worthwhile to note that the region referred to above as the "turbulent region" is mostly not fully turbulent and it is very unlikely that the turbulence is isotropic.

3. Conclusions

A direct numerical simulation of passive heat transfer in a laminar separation bubble flow over a flat plate with hot, oscillating oncoming flow has been performed. Some of the results were compared to an earlier simulation of LSB flow without passive heat transfer, where the inflow oscillations had an amplitude and a period that was twice as large (see also Table 1). The following conclusions are reached:

- In the simulations, every period a new separation bubble is formed and a spanwise turbulent roll of recirculating flow is shed.
- While in the earlier simulation (A), no merging of flow-separation regions was observed, in the present simulations the smaller period employed caused the remaining recirculation zone of the old separation bubble to merge with the newly formed bubble.
- The period between the onset of inflow acceleration and the peaks in the phase-averaged maximum reverse flow of Simulations A and B, respectively, is found to be approximately 0.30 time-units in both cases, while also the mean period of the Kelvin–Helmholtz instability is found to be independent of the period or the amplitude of the inflow velocity.
- For $x/L < 0.75$ good agreement is observed between the time and phase-averaged results of Simulations B and B.1. This is illustrated by plots of the time-averaged shape factor, the time-averaged skin-friction coefficient and the phase-averaged Nusselt number.
- The heat transfer to the plate is found to significantly increase in regions where hot outer fluid gets entrained in the recirculation region of the laminar separation bubble.
- Turbulence generated inside recirculating regions is found to inhibit the Nusselt number to drop below $Nu \approx 240$.
- Neither the turbulent viscosity hypothesis nor the temperature gradient-diffusion hypothesis is found to hold generally in the turbulent region of the phase-averaged flow.
- As a consequence, the turbulent Prandtl number shows significant deviations from its time-averaged value of $\sigma_T = 0.9$, reflected in a variance of 3.95. The same value of $\sigma_T = 0.9$ is usually employed in RANS simulations of boundary layer flow and would be a reasonable first approximation for the present flow problem too.

Acknowledgements

The authors would like to thank the German Research Foundation (DFG) for funding this project and the Computing Centre of the University of Karlsruhe for the computing time that was made available on the IBM SP-SMP.

References

Alam, M., Sandham, N.D., 2000. Direct numerical simulation of 'short' laminar separation bubbles with turbulent reattachment. J. Fluid Mech. 410, 1–28.

Breuer, M., Rodi, W., 1996. Large eddy simulations for complex turbulent flow of practical interest. In: Flow Simulations with High Performance Computers II, Notes in Numerical Fluid Mech., vol. 52.

Cebeci, T., Bradshaw, P., 1984. Physical and Computational Aspects of Convective Heat Transfer. Springer, New York.

Lou, W., Hourmouziadis, J., 2000. Separation bubbles under steady and periodic-unsteady main flow conditions. In: Proceedings of the 45th ASME International Gas Turbine and Aeroengine Technical Congress, Munich, Germany, May 8–11.

Maucher, U., Rist, U., Wagner, S., 1997. Secondary instabilities in a laminar separation bubbles. In: New Results in Numerical and Experimental Fluid Mechanics, NNFM 60, pp. 229–236.

Maucher, U., Rist, U., Wagner, S., 1999. Transition structures in a laminar separation bubble. In: NNFM, vol. 72, (Proceedings of 11th STAB/DGLR-Symposium, November 10–12, 1998), pp. 307–314.

Spalart, P.R., Strelets, M.Kh., 2000. Direct simulation of a turbulent boundary layer up to $Re_\theta = 1410$. J. Fluid Mech. 403, 329–349.

Wissink, J.G., 2003. DNS of separating, low-Reynolds number flow in a turbine cascade with incoming wakes. Int. J. Heat Fluid Flow 24, 626–635.

Wissink, J.G., Rodi, W., 2002. DNS of transition in a laminar separation bubble. In: Advances in Turbulence IX, Proceedings of the Ninth European Turbulence Conference, pp. 727–730.

Wissink, J.G., Rodi, W., 2003a. Direct numerical simulation of boundary layer separation along a curved wall with oscillating oncoming flow. In: High Performance Computing in Science and Engineering in Munich, 2002, pp. 113–123.

Wissink, J.G., Rodi, W., 2003b. DNS of a laminar separation bubble in the presence of oscillating flow. Flow, Turbulence and Combustion 17, 311–331.